AN ANALYSIS OF SYNTHETIC *SPITZER*/ IRAC LIGHT CURVES USING GAUSSIAN PROCESS REGRESSION

Jackson Hoffart,[1] Maximilien Lamberti,[1] Joel C. Schwartz,[1, 2, *] and Nicolas B. Cowan[1, 2, *]

[1]*Department of Physics, McGill University, 3600 rue University, QC, H3A 2T8, CAN*
[2]*Department of Earth and Planetary Science, McGill University, 3450 rue University, Montreal, QC, H3A 0E8, CAN*

ABSTRACT

The Infrared Array Camera (IRAC) aboard the *Spitzer* Space Telescope is a photometric instrument used frequently in the study of transiting exoplanets. The desired astrophysical signal can be small compared to the detector systematics. Accounting for instrumental systematics is thus imperative. Polynomial fits and bilinearly-interpolated subpixel sensitivity maps have been used to model intrapixel variability in the past. Gaussian process regression offers a more flexible approach to such an analysis, at the expense of computational complexity. Here, we present an analysis of simulated IRAC data using Gaussian processes. We fit noisy synthetic data to determine the astrophysical parameters. The median values for transit center, half-width, and relative depth were found to be $(12.01\,^{+0.49}_{-0.54})$ hrs, $(1.23\,^{+0.94}_{-0.53})$ hrs, $(7.5\,^{+4.4}_{-3.4}) \times 10^{-3}$ respectively, in agreement with the true values of 12.078 hrs, 0.89 hrs and 10.46×10^{-3}. The median values for eclipse half-width and relative depth were found to be $(2.5\,^{+3.2}_{-1.7})$ hrs and $(1.03\,^{+0.78}_{-0.57}) \times 10^{-3}$, in agreement with the true values of 0.72 hrs and 0.65×10^{-3}.

Keywords: infrared: planetary systems—instrumentation: detectors—methods: data analysis—methods: statistical

Corresponding author: Jackson Hoffart
jackson.hoffart@mail.mcgill.ca

Corresponding author: Maximilien Lamberti
maximilien.lamberti@mail.mcgill.ca

* Thesis Supervisors

1. INTRODUCTION

Extra solar planets (exoplanets) are planets which orbit stars beyond our solar system. While the term exoplanet has been in circulation since the 1940's, the first confirmed discovery of an exoplanet (51 Pegasi b) didn't occur for another 50 years (van den Bos 1943; Mayor & Queloz 1995), a delay that can be attributed to the exceedingly small scale of exoplanets in an astrophysical context. To highlight this size discrepancy, consider the volume of the Sun, which is on the order of 1.3×10^6 times greater than that of Earth (Carroll & Ostlie 2006).

Moreover, while stars emit formidable amounts of energy in the form of photons due to nuclear fusion, exoplanets offer no such intense signal (Carroll & Ostlie 2006). The study of exoplanets thus requires high instrumental sensitivity, and often we are only able to study the most massive and brightest exoplanets (so-called Hot Jupiters). Furthermore, the characterization of an exoplanetary system is often reliant on indirect methods (Ingalls et al. 2016).

Exoplanet transit photometry is one such method, used to infer characteristics of the system by measuring the flux emitted by the host star (Ingalls et al. 2016). When an exoplanet passes in front of or behind its host star with respect to the observer—referred to as primary transit and secondary eclipse respectively—characteristic signatures appear in the measured flux. By modelling these artifacts, we are able to infer numerous desirable characteristics. With respect to the stellar system, we can determine, for example, the planet-to-star radius ratio, orbital inclination and the ratio of semi-major axis to stellar radius (Krick et al. 2016). Similarly, characteristics relevant to the composition of the planet's atmosphere can be obtained, including the presence of water, methane, carbon monoxide or carbon dioxide (Evans et al. 2015).

Exoplanet photometry via thermal emission is most effectively studied at infrared wavelengths (Ingalls et al. 2016). The Infrared Array Camera (IRAC), aboard the *Spitzer* Space Telescope, has been used extensively to this end (e.g. Charbonneau et al. 2005; Deming et al. 2006; Knutson et al. 2007; Désert et al. 2009; Crossfield et al. 2012; Lewis et al. 2013; Todorov et al. 2014; Evans et al. 2015). That said, the photometric precision necessary for exoplanet photometry surpasses IRAC's design criteria, with relevant signals often being on the order of 100 parts per million (ppm) or smaller with respect to the background (Fazio et al. 2004; Ingalls et al. 2016). Significant consideration is thus required for IRAC systematics. One notable systematic found in the literature is non-uniform sensitivity across a single pixel (intrapixel variability) (Knutson et al. 2012). In May

2009, the cryogenic coolant present in *Spitzer* was depleted and the instrument entered its "warm phase", effectively doubling the amplitude of these sensitivity variations (Werner 2009; Ingalls et al. 2016).

Availability of space-based telescopes is often limited and highly competitive. As a result, observing time for a given project must usually be minimal, and dedicating time to instrumental calibration is often not feasible. Accordingly, self-calibration techniques are usually implemented (Krick et al. 2016). Early self-calibration techniques for modelling intrapixel variability fit radial functions to the center of a pixel (Reach et al. 2005). Polynomials were also fit to the position of the center of light (centroids) (Knutson et al. 2008). However, these methods could not sufficiently model the small scale structure present in the variations, especially if the variability was not smooth, or if significant correlations arose between detector parameters (Ingalls et al. 2016; Stevenson et al. 2012). A more responsive approach was outlined by Ballard et al. (2010) in which intrapixel variability was mapped onto a subpixel grid, with no assumption of the functional form. Stevenson et al. (2012) addressed some of the limitations of the scope of Ballard's method—predominately resulting from time constraints imposed by the complexity of the algorithm—and proposed a method known as Bilinearly-Inerpolated Sub-pixel Sensitivity (BLISS) mapping, which was computationally fast enough to be incorporated in a Markov Chain Monte Carlo (MCMC) (Stevenson et al. 2012). The BLISS method still fit a subpixel grid assuming no underlying functional form; however interpolation between knots within the grid was implemented via a method computationally less expensive than that implemented by Ballard (Stevenson et al. 2012).

A natural extension of the correlation techniques introduced with BLISS would be to analyze the data using a Gaussian process (GP) based kernel regression. Briefly, GP regression implements kernel functions to describe the covariance between data points, expressed as a covariance matrix (Rasmussen & Williams 2006). Using this matrix, a broad range of behaviours can be inferred from the underlying dataset (Rasmussen & Williams 2006; Evans et al. 2015). The main advantage to GP regression is that it can model correlations in the data that may not be understood from first principles by specifying only high-level properties of the covariance (Evans et al. 2015). Recently, GP models have been successfully applied to model transit light curves (e.g. Gibson et al. 2012a,b, 2013a,b; Evans et al. 2013; Gibson 2014).

In this paper, we analyze the efficacy of GP regression in fitting light curves and intrapixel variability to syn-

thetic IRAC data. The synthetic data models a typical exoplanet system, convolved with simulated IRAC systematics and photon noise. The paper's structure is as follows: In Section 2 we outline: 2.1 exoplanetary transit photometry, including the model used to generate our synthetic astrophysical data and 2.2 the *Spitzer*/ IRAC detector, its systematics and the model used to generate these synthetic systematics. In Section 3 we give a description of our method of analysis, Gaussian Process regression. Section 5 outlines the implications of our results, as well as prospects for future work. Finally, in Section 6, we give a brief summary of the paper.

2. THEORY

2.1. *Exoplanet Transit Photometry*

Exoplanet transit photometry is the indirect study of exoplanetary systems through measurements of the emitted flux of the host star with respect to time—'light curves'. As a toy model, consider an ideal star emitting constant flux in all directions (the stellar flux). The light curve of an ideal stellar flux will be a horizontal line, depicted as the yellow dashed line in Figure 2a.

Consider now the addition of an exoplanet to the toy model. When the planet passes in front of the star with respect to the detector, referred to as a primary transit, it will block some of the stellar flux, resulting in a reduction of the measured flux. The effect of a primary transit on the measured light curve can be seen as the large central dip in Figure 2a.

As the planet orbits the star, the side of the planet facing the star (the day side) is heated. The planet will re-emit this heat as thermal radiation, often at infrared wavelengths (IR) (Ingalls et al. 2016). As the planet passes around the star, the IR emission will add to the stellar flux, gradually increasing the measured flux. Immediately before the planet passes behind the star, the day side will be oriented toward the observer. The result is a maximum on the measured flux. When the planet passes behind the star, referred to as secondary eclipse, the thermal emission will drop and the measured flux will be the stellar flux alone. The effect of a secondary eclipse on the measured light curve is seen as the two smaller dips on either end of the light curve in Figure 2a.

We generate light curves using the model outlined in Schwartz & Cowan (2016). The model is a composite of the underlying flux, thermal IR variations, eclipse and transit effects. The functional form is lengthy and not exceptionally informative, so we will outline only the parameters involved in our analysis. The transit center, t_c, specifies the center time at which the transit occurs. Transit half-width, Δ_t, depicts the full-width half maximum value of the transit dip (similar for the eclipse half-width Δ_e). The transit depth, δ_t, gives the depth of the transit in terms of relative flux (similar for the eclipse depth δ_e).

2.2. *Spitzer/IRAC*

In the context of thermal emission, exoplanet transit photometry is most readily studied at infrared wavelengths (Ingalls et al. 2016). The Infrared Array Camera (IRAC) aboard the *Spitzer* Space Telescope is well suited to this task. The detector is composed of four channels measuring at central wavelengths of 3.6, 4.5, 5.8 and 8.0 μm. Each channel consists of an array of 256×256 detector pixels (Fazio et al. 2004).

IRAC systematics have been well-documented in the literature (e.g. Charbonneau et al. 2005; Agol et al. 2010; Stevenson et al. 2012). They are typically divided into two subsets: spatial intrapixel sensitivity fluctuations, characteristic of the 3.6 and 4.5 μm channels, and temporal detector ramp, observed in the 5.8 and 8.0 μm (Charbonneau et al. 2005; Evans et al. 2015). We focus on the intrapixel variability.

The 3.6 and 4.5 μm channels implement semiconducting pixel detectors made of indium antimonide (InSb) (Evans et al. 2015). In these channels, the measured flux correlates with position on the pixel. This effect is believed to be due to variations in quantum efficiency across a pixel (Evans et al. 2015).

While spatial resolution is limited by the number of pixels spanned by the stellar system, flux measurements from any given pixel tend to be precise. Systems of interest tend to be close, emitting considerable photon flux. The limiting error is due to photon counting, which follows Poisson statistics, scaling down as photon flux increases (for some value N of a counting experiment, the Poisson error scales as $\sqrt{N}$). By interpolating between flux measurements at each pixel, the position of the center of light within a pixel (centroid) can be determined (Ingalls et al. 2016). The center of light method interpolates flux as

$$x_c = \frac{\sum_i i\,(f_{ij} - f_{BG})}{\sum_i (f_{ij} - f_{BG})} \, , \qquad (1)$$

and

$$y_c = \frac{\sum_j j\,(f_{ij} - f_{BG})}{\sum_j (f_{ij} - f_{BG})} \, , \qquad (2)$$

where x_c, y_c are the centroids in the x and y position respectively, (i, j) is the pixel number, f_{ij} is the flux value at that pixel and f_{BG} is the background flux in the surrounding pixels. Sums are taken over a (7×7)-pixel region surrounding the expected position of the source (Ingalls et al. 2016).

The detector model simulates the inherent intrapixel sensitivity variations of IRAC. It incorporates variations in measured flux due to expansion and contraction effects as well as shifts in the centroid placement on a pixel due to small movements of the telescope, using the models outlined in Grillmair et al. (2014).

A plot of the centroid position in the x and y directions of an array of four pixels is seen in the left of Figure 1, while on the right is a simulated sensitivity map showing intrapixel variability.

3. GAUSSIAN PROCESSES

Broadly, Gaussian process (GP) regression involves defining a likelihood function in terms of astrophysical and systematic parameters, and maximizing it with respect to the data. GP regression differs from other regression algorithms in that—in addition to allowing for variance on any single data point—covariance is allowed between data points. This results in off-diagonals in the covariance matrix. These covariant terms are not static, and are optimized to the data. They can be used to account for systematics whose functional form may not be understood from first principles. Here, parameters are split into two classes: astrophysical parameters, defining the physical planetary system, and hyperparameters, used to describe systematics. The likelihood function depends on the residuals between the astrophysical model and data, and the covariance matrix. The covariance matrix is calculated using a so-called kernel function.

3.1. Kernel Functions

A kernel function is used to express similarity between data points. In our context, the purpose of the kernel function is to give a flexible description of the systematics. The choice of kernel for any given application therefore depends on the type of correlation expected in the data. Many classes of kernel function can be used, some of which are exotic and suited to very specific purposes (e.g. periodic kernels are implemented if periodic trends are expected in the covariance of the data).

A generic kernel is defined as

$$k = k(\boldsymbol{v}_i, \boldsymbol{v}_j) \;, \tag{3}$$

where $\boldsymbol{v}_i$ and $\boldsymbol{v}_j$ are the ith and j^{th} elements of the data input vector. In our analyses, $\boldsymbol{v}$ will be one of: the centroid position in x or y, or the time (x_c, y_c and t respectively). For elements of $\boldsymbol{v}_i$ and $\boldsymbol{v}_j$ which are close in value, k will return a value ~ 1, while for those that differ greatly in value, k will return ~ 0.

The kernel used to characterize the x- and y-position on the pixel is the squared exponential kernel:

$$k_{xy} = \omega_{xy}^2 \exp\left[- \left(\frac{x_i - x_j}{L_x} \right)^2 - \left(\frac{y_i - y_j}{L_y} \right)^2 \right], \tag{4}$$

where x_i and y_i are the centroid positions of the ith data point, L_x and L_y are the length scales over which intrapixel sensitivity variations are expected, and ω_{xy} is the weight associated with the kernel. This kernel indicates that, regardless of the functional form of the intrapixel variability, we expect similar regions of the pixel to exhibit similar sensitivity. Two points differing by several length scales, where systematics need not be related, would be assigned a covariance of 0.

To model temporal variations, the $\frac{3}{2}$-Matérn kernel was implemented, defined as:

$$k_t = \omega_t^2 \left(\sqrt{3} \, \frac{|t_i - t_j|}{L_t} \right) \exp\left[- \left(\sqrt{3} \, \frac{|t_i - t_j|}{L_t} \right) \right] \,, \tag{5}$$

where t_i is the corresponding time of the ith data point, L_t is the timescale over which we expect the centroid to move significantly, and ω_t is the weight associated with the kernel.

The squared exponential kernel accounts for smooth variations in the data, while the Matérn kernel accounts for residual correlated noise.

The effective kernel used in our analyses was the sum of these two kernels along with a term added to the diagonal, to account for Gaussian distributed noise in the data. This term effectively represents the variance of each data point due to photon noise, σ^2:

$$k = k_{xy} + k_t + \sigma^2 \, \delta_i^j, \tag{6}$$

where δ_i^j is the kronecker delta tensor. By applying the effective kernel to each combination of data points, a covariance matrix can be constructed as:

$$[\mathrm{K}_{ij}] = k(\boldsymbol{v}_i, \boldsymbol{v}_j) \tag{7}$$

Figure 3 shows two example covariance matrices calculated with k_{xy} and k_t respectively, as well as the final effective covariance matrix. Note that the hyperparameters for this example were not optimized to the data set. The covariance matrix $\mathbf{K}$ expresses all similarities in the data and is one of the main components of the GP likelihood function.

3.2. The Likelihood Function

In a GP, every data point is associated with a normally distributed random variable (Rasmussen & Williams 2006). The probability to measure
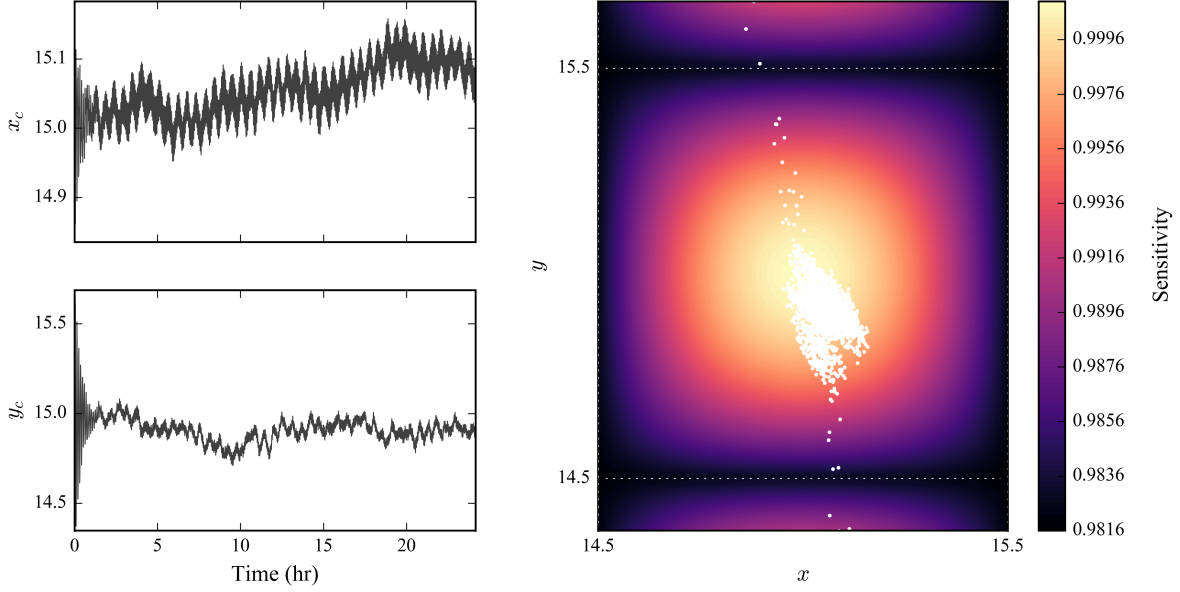
Figure 1. Synthetic IRAC data showing: (Left) Centroid position in x and y (in units of pixel side-length) with respect to time as determined by the center of light method. (Right) A map of intrapixel variability across three pixels (pixel boundaries are denoted by white). Sensitivity is in arbitrary units, normalized to the absolute flux of the star (no planet contribution). White points indicate samples of the centroid position over time. Synthetic data was generated using the method outlined in Schwartz & Cowan (2016). Data was simulated using the methods outlined in Grillmair et al. (2014).

dataset $\boldsymbol{d}$ $=$ $(d_1, ..., d_N)$ with standard deviation $\boldsymbol{\sigma}$ $=$ $(\sigma_1, ..., \sigma_N)$, given an underlying astrophysical model $\boldsymbol{A} = (A_1, ..., A_N)$ defined by parameters $\boldsymbol{\alpha}$ is

$$\mathcal{P}(\boldsymbol{d}|\boldsymbol{\alpha}) = \prod_{i=1}^{N} \frac{1}{\sqrt{2\pi\sigma_i^2}} \exp\left[-\frac{(d_i - A_i)^2}{2\sigma_i^2}\right] = \mathcal{N}(\boldsymbol{A}, \boldsymbol{\Sigma}) ,$$
(8)

where $\mathcal{N}$ is a multivariate normal distribution and $\boldsymbol{\Sigma} = \text{diag}[\boldsymbol{\sigma}]$ is the variance of the data, defined only along the diagonal. If we know modify this equation to include a covariance matrix with off-diagonals, as computed from equation 7, we obtain the following likelihood

$$\mathcal{P}(\boldsymbol{d}|\boldsymbol{\alpha}, \boldsymbol{\gamma}) = \mathcal{N}(\boldsymbol{A}, \mathbf{K} + \boldsymbol{\Sigma}) ,$$
(9)

where $\gamma = \{\omega_{xy}, \omega_t, L_x, L_y, L_t\}$ are the hyperparameters that define $\mathbf{K}$. Computationally it is easiest to optimize the logarithm of this function. The loglikelihood function is then

$$\ln\mathcal{P}(\boldsymbol{d}|\boldsymbol{\alpha}, \boldsymbol{\gamma}) = -\frac{1}{2}\left[\mathbf{r}^{\mathrm{T}}(\mathbf{K}+\boldsymbol{\Sigma})^{-1}\mathbf{r} + \ln|\mathbf{K} + \boldsymbol{\Sigma}| + N\ln(2\pi)\right] ,$$
(10)

where $\mathbf{r} = \boldsymbol{d} - \boldsymbol{A}$ is the residual vector between the data and the astrophysical model.

GP regression is effectively reduced to the optimization of Equation 10. However, it may not be clear why

this loglikelihood expression is a good framework to obtain estimates for $\boldsymbol{\alpha}$ and $\boldsymbol{\gamma}$. It is informative to break down the terms in equation 10 as

$$\ln\mathcal{P}(\boldsymbol{d}|\boldsymbol{\alpha}, \boldsymbol{\gamma}) = -\frac{1}{2}\left[\chi^2 + Penalty + Const\right].$$
(11)

The first term is a goodness-of-fit, similar to the χ^2. Its purpose is to minimize model residuals given the sensitivity of measurements encoded in $\mathbf{K}$. This term is also the most computationally expensive and problematic process in a GP, as it involves inverting a large $N \times N$ matrix, where N is the number of data points. This may become problematic when the matrix is sparse (as is often the case), and computationally scales on the order of $\mathcal{O}(N^3)$. The second term penalizes model complexity. If the length scales L_x, L_y, L_t become very small, this term decreases the likelihood, preventing overfitting. The GP regression therefore involves balancing the fit quality and model complexity. The final term is a normalization factor, which remains constant for a given dataset.

3.3. *Optimization*

According to Bayes theorem, the probability that a given data set will result in the astrophysical parameters
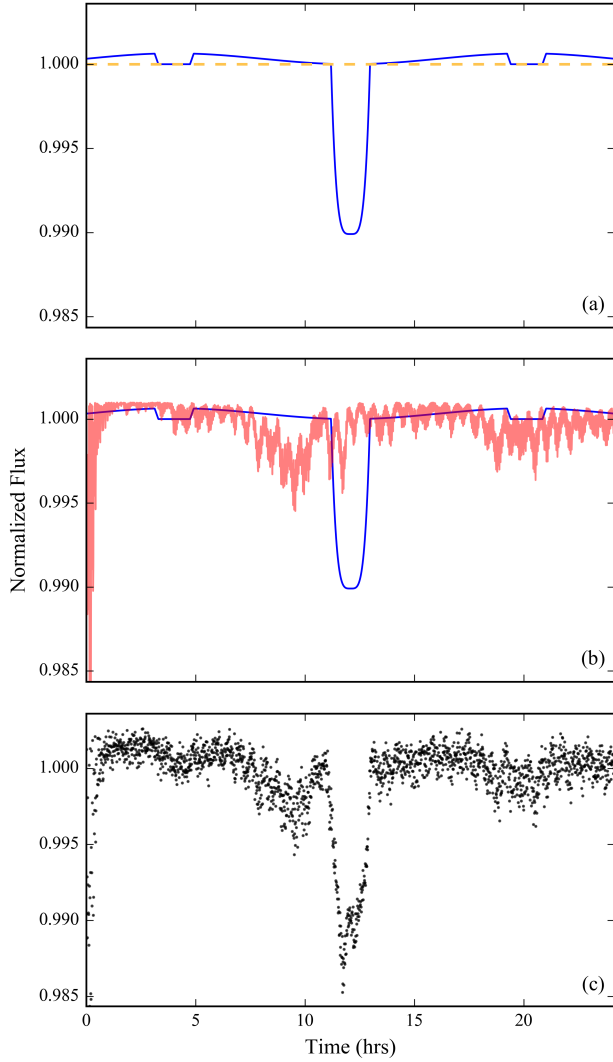
Figure 2. (a): Yellow dashed line depicts the constant stellar flux (no exoplanet contribution). Blue line shows a plot of the astrophysical model outlined in Schwartz & Cowan (2016). (b): Red line depicts the synthetically generated detector model, as outlined in Grillmair et al. (2014), superimposed on the astrophysical model (blue line). (c): Data points draw from the product of the astrophysical and detector model, with each data point having additional Gaussian distributed noise (representative of the photon noise).

$\boldsymbol{\alpha}$ and hyperparameters $\boldsymbol{\gamma}$ is given by:

$$\mathcal{P}(\boldsymbol{\alpha}, \boldsymbol{\gamma}|\boldsymbol{d}) \propto \mathcal{P}(\boldsymbol{d}|\boldsymbol{\alpha}, \boldsymbol{\gamma})\, \mathcal{P}(\boldsymbol{\alpha})\, \mathcal{P}(\boldsymbol{\gamma}) \ , \qquad (12)$$

where $\mathcal{P}(\boldsymbol{d}|\boldsymbol{\alpha}, \boldsymbol{\gamma})$ is the loglikelihood from equation 10 and $\mathcal{P}(\boldsymbol{\alpha})$ and $\mathcal{P}(\boldsymbol{\gamma})$ are the respective prior probability distributions (priors) of the astrophysical and hyperparameters.

Uniform priors were chosen for all optimization variables. The bounds for the astrophysical parameters were applied liberally to be between 0 and 10 times the true

value of the parameter, or in case of the phase offset within $\pm\pi/2$, which encompasses all values accessible to the astrophysical model. The bounds for the hyperparameters were between 0 and 2 for the weights ω_i, 0 and 1 for the spatial length scales L_x and L_y, 0 and the total observation time of a data set for the temporal length scale L_t, and 0 and 1 for the noise σ.

At the beginning of an optimization process, initial values for the astrophysical- and hyperparameters were drawn randomly from the priors. The drawn values were used to initialize a Nelder-Mead Simplex optimization algorithm—using the `Lmfit` python library— to obtain maximum likelihood estimates (MLE) of Equation 10 (Nelder & Mead 1965; Newville et al. 2014). Since the covariance matrix had to be recomputed and inverted at each new iteration of hyperparameters, the optimization routine turned out to be computationally expensive and was prone to over- and underflow errors. An efficient and numerically stable computation was achieved by applying a Cholesky decomposition, which exploits the positive-definite property of the covariance matrix and solves the inversion problem as a system of linear equations.

The Nelder-Mead optimization was repeated ten times, with different parameter initializations at each repetition. This was done to prevent optimizing to a local minimum of the likelihood surface. From the ten optimization routines, the parameters of the run which maximized the likelihood were chosen and used for further analysis.

In order to make the following sampling routines computationally tractable, the hyperparameters were kept fixed at their MLEs from this point onward. It should be noted however, that fixing the hyperparameters is not analogous to fixing the parameters of an explicit functional systematic model, but instead amounts to selecting a family of parametric models to characterize the high-level properties of the systematics (Evans et al. 2015).

For additional exploration of the likelihood space as well as obtaining error estimates for the astrophysical parameters, an MCMC Ensemble Sampler was implemented using the python library `emcee` (Foreman-Mackey et al. 2013; Goodman & Weare 2010). 10 walkers per parameters were used for any given optimization routine. The walkers were initialized in a small locus around the MLEs of the parameters determined by the previous Nelder-Mead optimization. With these general guidelines in mind, the transit and eclipse parameters were then fit separately for a more efficient exploration of the parameter space. The resulting sample chains
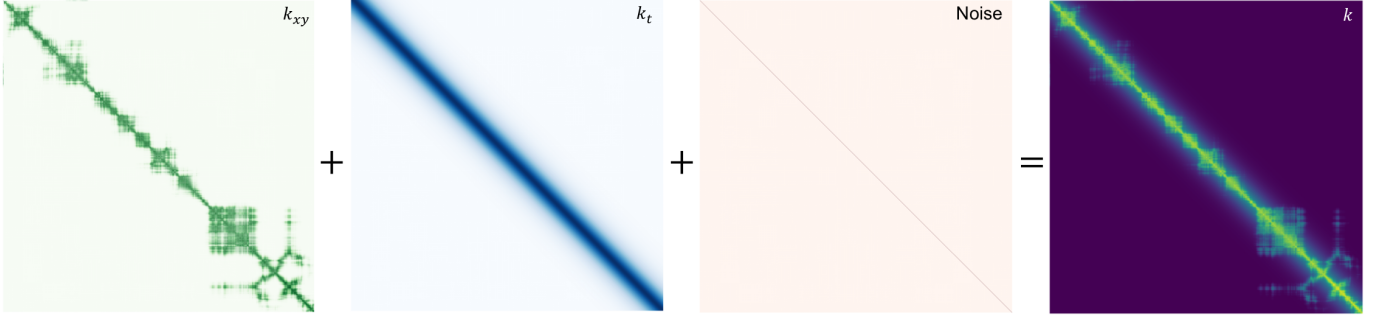
Figure 3. From left to right: Plots of the squared exponential kernel (k_{xy}), the $\frac{3}{2}$-Matérn kernel (k_t), Gaussian noise (*Noise*) and the sum of the three, (k). Colour saturation indicates high correlation. The final effective covariance matrix, k, should contain all information regarding pixel systematics.

were then cleaned by truncating an initial period and slicing to eliminate autocorrelations.

4. RESULTS

Regarding the transit, we ran an MCMC to sample the following parameters: the transit center, t_c, the transit half-width, Δ_t, and the transit depth, δ_t. The posterior distribution obtained from sampling the space of transit parameters is shown in Figure 4. We quote the median values, with errors ranging the central 68% spread, in Table 1.

In regard to the secondary eclipse, the MCMC was sampled for the following parameters: the eclipse half-width, Δ_e, and the eclipse depth, δ_e. The posterior distribution obtained from sampling the space of eclipse

parameters is shown in Figure 5. We quote the median values, with errors ranging the central 68% spread, in Table 2.

Due to the skew nature of the probability distribution, the MLEs do not coincide with the median probability parameters. As such, we have quoted the median values, with errors defined by the values encompassing 68% of the data in Tables 1 and 2. Alternatively, our best fit parameters are given by the MLEs, which have less reliable error estimates. The MLEs for the astrophysical and hyperparameters are shown in Table 3. The best fit
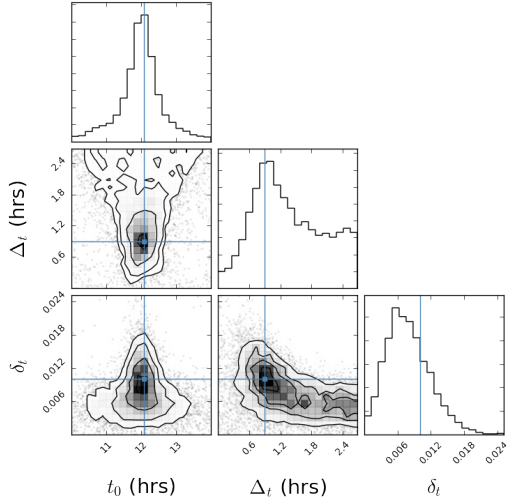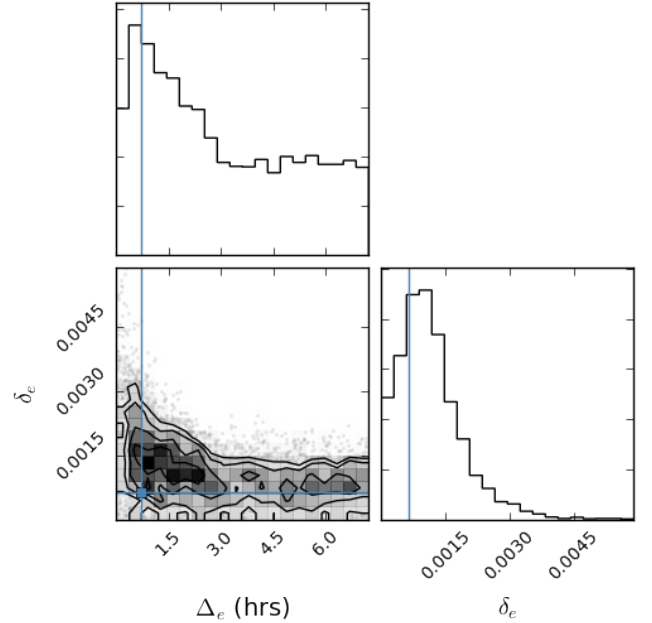

Figure 4. The posterior distribution of the transit parameters from the MCMC chains. The contour plots indicate the density of samples of two given parameters while the histograms show the marginalized distribution for each individual parameter. t_c is the transit center, Δ_t is the transit half-width and δ_t is the transit depth in units of normalized flux. The blue lines indicate the position of the true synthetic values.

Figure 5. The posterior distribution of the eclipse parameters from the MCMC chains. The contour plots indicate the density of samples of two given parameters while the histograms show the marginalized distribution for each individual parameter. Δ_e is the eclipse half-width and δ_e is the eclipse depth in units of normalized flux. The blue lines indicate the position of the true synthetic values.
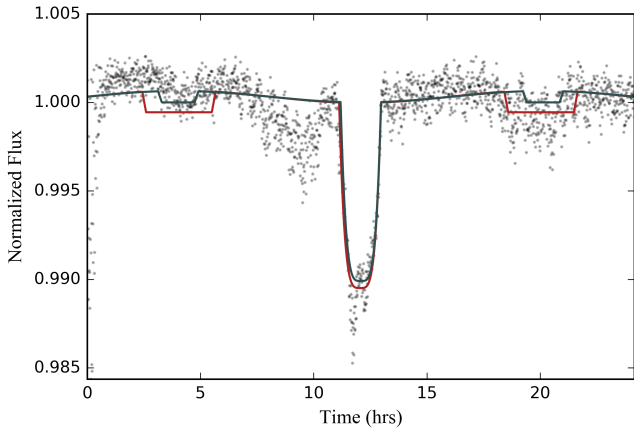
Figure 6. Blue curve depicts the true synthetic astrophysical model. Black points show the full synthetic data, being a combination of the astrophysical model, detector model and photon noise. The red curve is our best fit model, using the parameters which maximized the loglikelihood function.

curve is plotted in Figure 6 along with the original light curve generated with the true values.

5. DISCUSSION

Figure 6 shows our final best-fit astrophysical model, in comparison to the true synthetic model used to generate the data. The parameters describing the transit are closer to the genuine values than are the eclipse parameters. The can most likely be explained by how weak the eclipse signal is in comparison to the signal of the transit, potentially to such a degree that sensitivity variations and noise become dominant for the eclipse signal. We consider how the type of Gaussian process regression presented here can be applied to future experiments.

IRAC's 5.8 and 8.0 μm channels implement silicon arsenic (Si:As) as the semi-conducting material (Evans et al. 2015). An effect known as detector ramp has been observed in these detectors, in which the measured flux smoothly increases or decreases with time before reaching a steady-state value (Evans et al. 2015). In the 8.0 μm channel, this effect has been attributed to charge trapping, where photons saturate traps in the detector and thus increase the overall flux of electrons (Knutson et al. 2009). It has been acknowledged, however, that theoretical models of these detectors are lacking, and systematics observed in the 5.8 μm detector remain unexplained (Seager & Deming 2010).

In principle, the GP regression model outlined in this paper could be extended to model these detector ramp systematics. This could be done by including in the effective kernel an exponential squared kernel, dependent on some parameter describing the timescale of the ramp effect. This kernel should be able to encode the steep

initial increase/decrease of sensitivity with respect to time, followed by the level-off (Evans et al. 2015).

Modelling detector ramp effect would also be useful for the next generation of instruments. The James Webb Space Telescope (JWST) is a project led by the NASA with major contributions from the European and Canadian Space Agencies (ESA and CSA) (Gardner et al. 2006). It is a space-based observatory, that will measure at infrared (IR) wavelengths ($\sim 0.6-28.5$ μm) (Gardner et al. 2006). As such, it will be of paramount use to exoplanet studies. The Mid-Infrared Instrument (MIRI) aboard the JWST will be the most well-suited instrument to study exoplanet transit photometry. Similar to *Spitzer*/ IRAC's 5.8 and 8.0 μm channels, MIRI will be composed of Si:As detectors, arranged in an extended 1024×1024 pixel format (Rieke et al. 2015). We expect these detectors to exhibit similar detector ramp effects as those described above and thus a similar extension of our method could apply to data from this instrument.

Table 1. Results of the MCMC chains for the transit parameters. The values quoted are the median of each of the chains with ranges indicating the central 68% spread of the samples around the median.

t_0 (hrs)	Δ_t (hrs)	δ_t
$12.01^{+0.49}_{-0.54}$	$1.23^{+0.94}_{-0.53}$	$(7.5^{+4.4}_{-3.4}) \times 10^{-3}$

Table 2. Results of the MCMC chains for the eclipse parameters. The values quoted are the median of each of the chains with ranges indicating the central 68% spread of the samples around the median.

Δ_e (hrs)	δ_e
$2.5^{+3.2}_{-1.7}$)	$(1.03^{+0.78}_{-0.57}) \times 10^{-3}$

6. CONCLUSION

In this paper, we have presented an analysis of synthetic *Spitzer*/ IRAC exoplanet light curves using Gaussian Process regression. The median values for transit center, half-width, and relative depth were found to be $(12.01^{+0.49}_{-0.54})$ hrs, $(1.23^{+0.94}_{-0.53})$ hrs, $(7.5^{+4.4}_{-3.4}) \times 10^{-3}$ respectively, in agreement with the true values of (12.078) hrs, (0.89) hrs and 10.46×10^{-3}. The median values for eclipse half-width and relative depth were found to be $(2.5^{+3.2}_{-1.7})$ hrs and $(1.03^{+0.78}_{-0.57}) \times 10^{-3}$, in agreement with the true values of (0.72) hrs and 0.65×10^{-3}. We conclude that Gaussian process regression offers a viable alternative for IRAC light curve fitting.

Table 3. Table of the MLEs for each parameter (hyper-, transit and eclipse). The true values of the astrophysical parameters are shown for comparison.

	ω_{xy}	L_x	L_y	ω_t	L_t	σ	t_0	Δ_t	δ_t	Δ_e	δ_e
	(%)	(pix)	(pix)	(%)	(mins)	(ppm)	(hrs)	(hrs)		(hrs)	
MLE:	99.96	1.078×10^{-4}	1.327×10^{-3}	13.98	3.667	2890	$12.050^{+0.47}_{-0.41}$	0.92	1.046×10^{-2}	1.45	1.22×10^{-3}
True:	—	—	—	—	—	—	12.078	0.89	1.009×10^{-2}	0.72	0.65×10^{-3}

7. ACKNOWLEDGEMENTS

REFERENCES

Agol, E., Cowan, N. B., Knutson, H. A., et al. 2010, ApJ, 721, 1861

Ballard, S., Charbonneau, D., Deming, D., et al. 2010, PASP, 122, 1341

Carroll, B. W., & Ostlie, D. A. 2006, Institute for Mathematics and Its Applications,

Charbonneau, D., Allen, L. E., Megeath, S. T., et al. 2005, ApJ, 626, 523

Crossfield, I. J. M., Knutson, H., Fortney, J., et al. 2012, ApJ, 752, 81

Deming, D., Harrington, J., Seager, S., & Richardson, L. J. 2006, ApJ, 644, 560

Désert, J.-M., Lecavelier des Etangs, A., Hébrard, G., et al. 2009, ApJ, 699, 478

Evans, T. M., Pont, F., Sing, D. K., et al. 2013, ApJL, 772, L16

Evans, T. M., Aigrain, S., Gibson, N., et al. 2015, MNRAS, 451, 680

Fazio, G. G., Hora, J. L., Allen, L. E., et al. 2004, ApJS, 154, 10

Foreman-Mackey D., Hogg D. W., Lang D., Goodman J., 2013, PASP, 125, 306

Gardner, J. P., Mather, J. C., Clampin, M., et al. 2006, SSRv, 123, 485

Gibson, N. P., Aigrain, S., Pont, F., et al. 2012, MNRAS, 422, 753

Gibson, N. P., Aigrain, S., Roberts, S., et al. 2012, MNRAS, 419, 2683

Gibson, N. P., Aigrain, S., Barstow, J. K., et al. 2013, MNRAS, 428, 3680

Gibson, N. P., Aigrain, S., Barstow, J. K., et al. 2013, MNRAS, 436, 2974

Gibson, N. P. 2014, MNRAS, 445, 3401

Goodman, J. & Weare, J. 2010, Comm. App. Math. Comp. Sci., 5, 65

Grillmair, C. J., Carey, S. J., Stauffer, J. R., & Ingalls, J. G. 2014, Proc. SPIE, 9143, 914359

Ingalls, J. G., Krick, J. E., Carey, S. J., et al. 2016, AJ, 152, 44

Knutson, H. A., Charbonneau, D., Allen, L. E., et al. 2007, Nature, 447, 183

Knutson, H. A., Charbonneau, D., Allen, L. E., Burrows, A., & Megeath, S. T. 2008, ApJ, 673, 526-531

Knutson, H. A., Charbonneau, D., Cowan, N. B., et al. 2009, ApJ, 703, 769

Knutson, H. A., Lewis, N., Fortney, J. J., et al. 2012, ApJ, 754, 22

Krick, J. E., Ingalls, J., Carey, S., et al. 2016, ApJ, 824, 27

Lewis, N. K., Knutson, H. A., Showman, A. P., et al. 2013, ApJ, 766, 95

Mayor, M., & Queloz, D. 1995, Nature, 378, 355

Nelder, J. A. & Mead, R. 1965, Computer Journal, 7, 308

Newville M., Stensitzki T., Allen D., Ingargiola A., 2014, Zenodo

Rasmussen, C. E., Williams, C. K. I. 2006, Gaussian Processes for Machine Learning (Cambridge, Massachusetts, USA: MIT Press)

Reach, W. T., Megeath, S. T., Cohen, M., et al. 2005, PASP, 117, 978

Rieke, G. H., Ressler, M. E., Morrison, J. E., et al. 2015, PASP, 127, 665

Schwartz, J. C., & Cowan, N. B. 2016, arXiv:1607.01013

Seager, S., & Deming, D. 2010, ARA&A, 48, 631

Stevenson, K. B., Harrington, J., Fortney, J. J., et al. 2012, ApJ, 754, 136

Todorov, K. O., Deming, D., Burrows, A., & Grillmair, C. J. 2014, ApJ, 796, 100

van den Bos, W. H. 1943, Monthly Notes of the Astronomical Society of South Africa, 2, 14

Werner, M. 2009, American Scientist, 97, 458